Ann Nucl Med (2014) 28:512–522
DOI 10.1007/s12149-014-0841-x

ORIGINAL ARTICLE

Effect of surrounding materials on iterative reconstruction-based line-source response function, and annihilations outside the source assessed by a small animal PET scanner

Yoshiharu Miyazaki · Masato Kobayashi · Ryoko Komatsu · Akiko Hayashi · Shoko Yonezawa · Keiichi Kawai · Masamichi Matsudaira · Jun Shiozaki · Ichiro Matsunari

Received: 23 July 2013 / Accepted: 13 March 2014 / Published online: 29 March 2014

Abstract
Objective The aims of this study were (1) to evaluate the effect of surrounding materials on the iterative reconstruction-based line-source response function (IR-RF) of ^{18}F, ^{11}C, ^{13}N, and ^{15}O using a preclinical PET system, and (2) to determine whether and how annihilation outside the source can be visualized experimentally.
Methods We performed all the measurements using the LabPET-8 PET/CT subsystem built-in the Triumph II platform (TriFoil Imaging, Inc., Northridge, CA, USA). IR-RF was measured for ^{18}F, ^{11}C, ^{13}N, and ^{15}O, and was expressed as full-width at half-maximum (FWHM) and full-width at tenth maximum (FWTM) using a glass capillary phantom mounted in materials of various densities, which were chosen to cover the wide range of real tissues. To determine whether and how annihilation outside the source can be visualized, we designed a concentric ring paper phantom, which consisted of a source at the center with 4 ring-like paper layers.
Results When the radionuclides were placed in air (material density 0 g/cm^3), IR-RFs were similar among the radionuclides tested. As the surrounding material density increased, IR-RFs for higher energy-emitting radionuclides (^{11}C, ^{13}N, and ^{15}O) became worse, whereas those of ^{18}F remained relatively constant over the range of surrounding material densities (0–2.17 g/cm^3). Both FWHM and FWTM values were closely correlated with mean energy of radionuclides at middle to high material densities (material density 0.94–2.17 g/cm^3). The FWTM/FWHM ratio of high energy-emitting radionuclides such as ^{15}O increased as a function of material density, which was followed by subsequent decrease at high material densities (1.2–2.17 g/cm^3). Using a concentric ring paper phantom, annihilations outside the source were visible and measurable. The innermost layer was visible with all radionuclides, whereas the outer layers only with high energy positron emitters.
Conclusions The results indicate that surrounding material affects IR-RF particularly for high energy positron emitters. Furthermore, annihilation outside the radio-active source can be visualized with some circumstances such as those seen with a concentric ring paper phantom.

Keywords Iterative reconstruction-based spatial resolution · Positron range · Surrounding materials · PET · Annihilation

Y. Miyazaki · R. Komatsu · A. Hayashi · S. Yonezawa · M. Matsudaira · I. Matsunari (✉)
Clinical Research Department, The Medical and Pharmacological Research Center Foundation, Wo 32, Inoyama, Hakui, Ishikawa 925-0613, Japan
e-mail: matsunari@mprcf.or.jp

M. Kobayashi · K. Kawai
School of Health Sciences, College of Medical, Pharmaceutical and Health Sciences, Kanazawa University, Kodatsuno 5-11-80, Kanazawa, Ishikawa 920-0942, Japan

J. Shiozaki
Department of Nuclear Medicine, Noto General Hospital, Abu 6-4, Fujihayashi-machi, Nanao, Ishikawa 926-0816, Japan

Introduction

Preclinical molecular imaging such as PET using small animals is increasingly being recognized as an important tool for biomedical research and new drug development [1, 2]. Although the state-of-the-art preclinical PET systems have reportedly achieved near millimeter spatial resolutions [3], it is still a limiting factor to image very small structures such as those encountered in mouse organs.

Spatial resolution is known to be affected by several factors such as positron range, non-colinearity of annihilating photons, and intrinsic properties of the PET scanner. The overall spatial resolution of the systems is a convolution of these components. Tissue surrounding the radioactive source is another important factor that affects spatial resolution as demonstrated in a MonteCarlo simulation study by Sanchez-Crespo et al. [4]. To date, however, the effect of surrounding materials on spatial resolution for positron emitters with different flight ranges has not yet been investigated systematically in experimental studies, except for one by Kemerink et al. [5] who investigated the effect of positron range of ^{18}F, ^{68}Ga and ^{124}I on PET in lung equivalent materials.

Apart from possible spatial resolution deterioration due to positron range, annihilation outside the source may create hot regions where the radioactive source does not exist. If this is true, such a phenomenon could be a problem in image interpretation, because the positron range of some radionuclides such as ^{11}C, ^{13}N, or ^{15}O exceeds the spatial resolution of modern preclinical PET scanners [3]. However, whether such annihilation outside the source can be visualized has not been well documented in literature.

The aims of this study were (1) to evaluate the effect of surrounding materials on the iterative reconstruction-based line-source response function (IR-RF) of ^{18}F, ^{11}C, ^{13}N, and ^{15}O positron emitters using a preclinical PET system, and (2) to determine whether and how annihilation outside the source can be visualized experimentally. We used IR-RF as a term referring to spatial resolution obtained in the present study, because we used iterative reconstruction rather than filtered back projection (FBP). We chose ^{18}F, ^{11}C, ^{13}N, and ^{15}O as radionuclides to be tested in this study because they are commonly used, have different positron ranges, and are pure or near pure positron emitters. To address the second issue, we designed a concentric ring paper phantom as detailed in a later section.

Methods

System description

We performed all the measurements using the LabPET-8 PET/CT subsystem built-in the Triumph II platform (TriFoil Imaging, Inc., Northridge, CA, USA), which is a preclinical imaging system dedicated for small animal imaging. The features and performance of this imaging system were described in detail elsewhere [6]. In brief, the detector array consisted of 6144 crystals arranged in contiguous rings with a ring diameter of 16.2 cm and an axial field of view (FOV) of 7.5 cm. The scintillation crystals were composed of an assembly of Lu0.4Gd1.6SiO5 (LGSO) and Lu1.9Y0.1SiO5 (LYSO) with dimensions of 2 2 14 mm. All PET studies were acquired using a 250–650 keV energy window and 22 ns coincidence-timing window.

Reconstruction settings

The list-mode data were binned into three-dimensional (3D) histograms or sinograms. The images were reconstructed using the 3D ordered subset expectation maximization (OSEM) algorithm with 1 subset and 100 iterations according to the recommendations by the manufacturer. The voxel size was set to the smallest one available in this system (0.25, 0.25, 0.5 mm) using a high-resolution mode option. The use of 3D OSEM rather than FBP in this study was because of two reasons. Firstly, FBP in our system had very limited capability in that it provided no options for filter selection and filter parameters. Secondly, the high-resolution option was not available for FBP in our system; the voxel size was always set to 0.5, 0.5, 0.5 mm with FBP instead of 0.25, 0.25, 0.5 mm with 3D OSEM. For these reasons, the use of iterative reconstruction rather than FBP is recommended for routine imaging by the manufacturer. The acquired data were not corrected for attenuation or scatter and reconstructed without post-reconstruction smoothing unless specified. However, CT-based attenuation with or without scatter correction was performed for iterative reconstruction-based spatial resolution measurements with the high density material as mentioned later.

Positron emitting radionuclides

Radionuclides were provided as a form of ^{18}F-fluorodeoxyglucose, ^{11}C-acetate, ^{13}N-ammonia, or ^{15}O-water. Physical characteristics of the radionuclides are summarized in Table 1.

Table 1 Physical characteristics of ^{18}F, ^{11}C, ^{13}N, and ^{15}O

	^{18}F	^{11}C	^{13}N	^{15}O
Half-life (min)	109.8	20.4	9.98	2.03
Decay mode	97 % β^+	100 % β^+	100 % β^+	100 % β^+
Maximum energy (MeV)	0.69	0.96	1.19	1.7
Mean energy (MeV)	0.250	0.386	0.492	0.735
Maximum range in water (mm)	2.4	4.1	5.4	8.0

The physical characteristics of radionuclides are based on data from Health Physics Society [7] and International Commission on Radiation Units and Measurements [8]

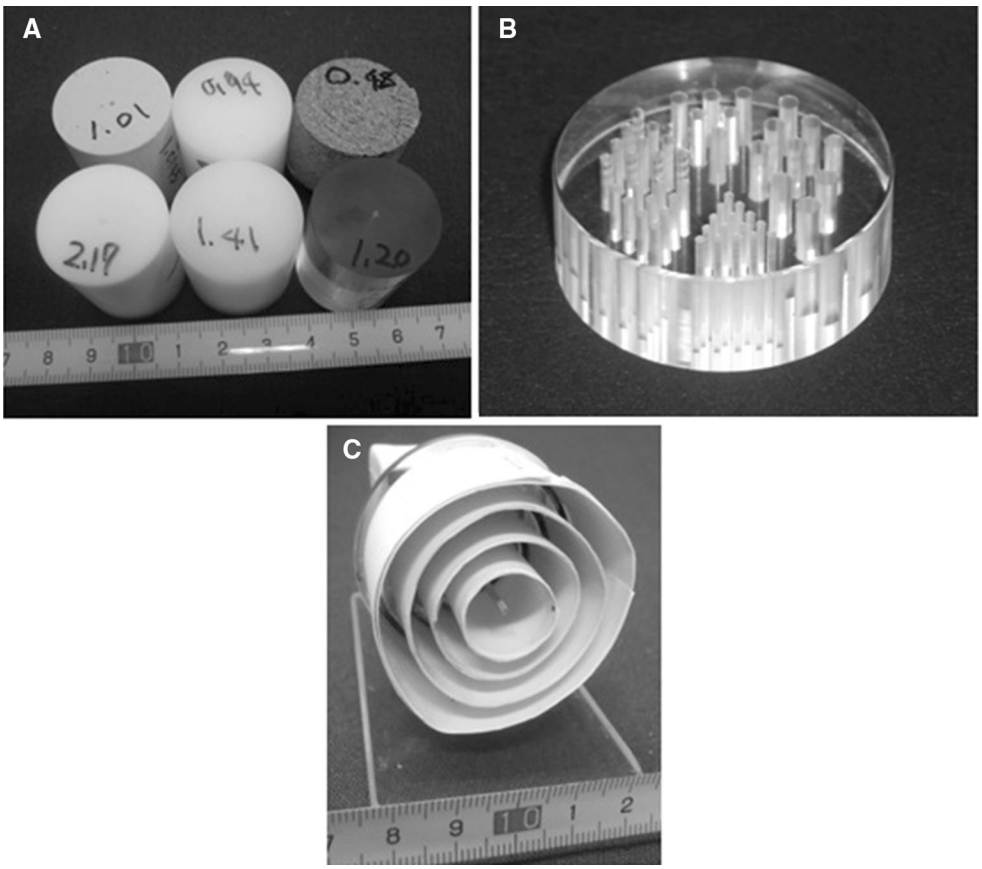

Fig. 1 Phantoms simulating surrounding tissue of various densities (**a**); the EP resolution phantom (**b**); a concentric ring paper phantom (**c**)

Iterative reconstruction-based line-source response function measurements

For IR-RF measurements with various surrounding materials, a glass capillary of inner diameter 0.14 mm (outer diameter 0.55 mm) was filled with solution of ^{18}F-fluorodeoxyglucose (mean ± standard deviation of 35 acquisitions for each radionuclide: 227 ± 111 MBq/mL), ^{11}C-acetate (239 ± 120 MBq/mL), ^{13}N-ammonia (316 ± 171 MBq/mL), or ^{15}O-water (1801 ± 500 MBq/mL) at the start of acquisition. The glass capillary line source was then placed in air (material density 0 g/cm^3) or one of the 6 cylindrical tissue phantoms (30-mm in length and 25.4-mm in diameter) (Hokuriku EP, Hakui, Japan) (Fig. 1a) in the center of FOV. The cylindric tissue phantoms were made of compressed cork (material density 0.48 g/cm^3), polyethylene (material density 0.94 g/cm^3), mixture of paraffin, polyethylene, pine resin, magnesium oxide, and titanium dioxide (material density 1.01 g/cm^3), polycarbonate (material density 1.20 g/cm^3), polyacetal (material density 1.41 g/cm^3), or polytetrafluoroethylene (material density 2.17 g/cm^3). These materials were chosen to cover the wide range of real tissues (e.g., air 0 g/cm^3, adipose tissue 0.92 g/cm^3, soft tissue 1.0 g/cm^3, bone 1.85 g/cm^3) [4]. A cylindric hole (diameter, 0.6 mm) was drilled at the center of each tissue phantom so that the capillary line source fitted inside and in the center of FOV. Additionally, these measurements were performed for a ^{11}C-line source (150 ± 70 MBq/mL) with a radial offset of 25 mm to assess measurement stability over transaxial FOV.

PET acquisition was performed 5 times for each surrounding material, resulting in a total of 35 acquisitions for each radionuclide. The acquisition time was 10 min for ^{18}F, ^{11}C, and ^{13}N, and 5 min for ^{15}O. To assess the influence of attenuation/scatter correction on measurements, CT scan for approximately 1 min was additionally performed for ^{11}C with the highest density surrounding material (material density 2.17 g/cm^3). The full-width at half-maximum (FWHM) and full-width at tenth of maximum (FWTM) were determined by linear interpolation between adjacent pixels at half or one-tenth of the maximum value of the line count profile on the reconstructed transaxial image based on the National Electrical Manufacturers Association (NEMA) NU4-2008 recommendation [9]. The maximum value was determined by a parabolic fit using the peak point and its two nearest neighboring points,

respectively. The averages of radial and tangential directions were calculated over 10 transaxial slices for all 35 acquisition data for each radionuclide.

Resolution phantom measurements

To have an overview of how IR-RF looks like visually, we performed imaging using the EP resolution phantom (Hokuriku EP, Hakui, Japan) (Fig. 1b). The phantom was made of acrylic resin (density 1.19 g/cm^3) with dimensions of 27 mm in diameter and 10 mm in height. It had 6 segments with fillable capillary rods of 0.7, 0.9, 1.0, 1.3, 1.5, and 1.8 mm in diameter with the distances between the capillary rods in a segment equal to the capillary diameter within that segment. The phantom was filled with 48.5 MBq of ^{18}F-fluorodeoxyglucose, 109 MBq of ^{11}C-acetate, or 133 MBq of ^{13}N-ammonia, and was then scanned for 60 min for ^{18}F, 30 min for ^{11}C, and 20 min for ^{13}N. We could not test ^{15}O imaging in a reliable manner because the very short half-life (2 min) of this radionuclide prevented us from completion of the phantom preparation, which usually took approximately 10 min.

Concentric ring paper phantom

To determine whether and how annihilation outside the source can be visualized, we designed a concentric ring paper phantom as depicted in Fig. 1c. The phantom consisted of a source at the center with 4 ring-like paper layers (15, 25, 35 and 45 mm in diameter). Each layer consisted of 6 sub-layers of 90-μm thick papers. A filter paper chip, which served as a source at the center, was infiltrated with 1.2 ± 0.5 MBq of ^{18}F-fluorodeoxyglucose, 1.2 ± 0.5 MBq of ^{11}C-acetate, 1.5 ± 0.9 MBq of ^{13}N-ammonia, or 0.5 ± 0.5 MBq of ^{15}O-water, and was then scanned for 30 min for ^{18}F, 20 min for ^{11}C, 10 min for ^{13}N, and 5 min for ^{15}O, followed by X-ray CT scan. PET/CT acquisition was performed 5 times for each radionuclide. The idea behind this experiment is that (1) in general, positrons travel long distances (i.e., several meters) in air; (2) however, in the presence of light materials such as paper, some positrons might be trapped with annihilations; (3) such annihilations could be detected using preclinical PET imaging; (4) the amount of annihilations on each layer would depend on the energy of positron emitters and the distance between the source and the paper layer. Furthermore, 5 additional acquisitions were performed for ^{18}F with the source covered with a 3-mm-thick clay (material density 2.10 g/cm^3) to see the effect of high-density materials on annihilation. On reconstructed transaxial images, total count of the source at the center or each layer was obtained using AMIDE software [10] for all 5 acquisitions for each radionuclide. On the basis of these count values, layer-to-center count ratios were calculated for each layer as follows: total count of a layer/total count of source at the center.

Statistical analysis

Values for repeated measurements were expressed as mean ± 1 standard deviation. Statistical analysis was performed using JMP 10 (SAS Institute Inc. Cary, NC, USA), or GraphPad Prism 6 (GraphPad Software, Inc. San Diego, CA, USA), where appropriate. Comparisons of mean values were performed using t test or analysis of variance (ANOVA), followed by Tukey's multiple comparison test. Correlations of variables were analyzed by simple linear regression, which were done only when the variable was significantly different. Statistical significance was defined as $P < 0.05$.

Results

Iterative reconstruction-based line-source response function

The IR-RFs expressed as FWHM/FWTM for ^{18}F, ^{11}C, ^{13}N, and ^{15}O in relation to surrounding material density are summarized in Table 2. When the radionuclides were placed in air (material density 0 g/cm^3), IR-RFs were similar among the radionuclides tested. In particular, FWHM values were below 1 mm for all the radionuclides when the sources were placed at the center of FOV. As the material density increased, IR-RFs for higher energy-emitting radionuclides (^{11}C, ^{13}N, and ^{15}O) became worse, whereas those of ^{18}F remained relatively constant over the range of surrounding material densities tested (0–2.17 g/cm^3). The worst FWHMs were observed at material density of 0.94 g/cm^3 for ^{18}F, 1.01 g/cm^3 for ^{11}C, 2.17 g/cm^3 for ^{13}N, and 2.17 g/cm^3 for ^{15}O, whereas the worst FWTMs were at material density of 0.94 g/cm^3 for ^{18}F, 1.20 g/cm^3 for ^{11}C, 0.94 g/cm^3 for ^{13}N, and 1.01 g/cm^3 for ^{15}O. The use of attenuation and scatter correction slightly but significantly improved FWHM and FWTM in the presence of high density surrounding material, whereas the use of attenuation correction alone did not. When the ^{11}C source was placed 25 mm off-center, both FWHM and FWTM were significantly but only modestly (e.g., 20 ± 6 % in FWHM) worse than those obtained at the center of FOV with most surrounding materials tested. The FWTM/FWHM ratios are plotted for each radionuclide as a function of material density in Fig. 2. At low to middle material density (0–1.01 g/cm^3), the FWTM/FWHM ratio of high energy-emitting radionuclides such as ^{15}O increased as a function of material density, which was followed by subsequent decrease at high material densities (1.2–2.17 g/

Table 2 Full-width at half-maximum (FWHM) and full-width at tenth of maximum (FWTM) (parenthesis) values for ^{18}F, ^{11}C, ^{13}N, and ^{15}O in relation to surrounding material density

	^{18}F	^{11}C	^{13}N	^{15}O	*P* value by ANOVA	^{11}C off-center (25 mm)
Material density (g/cm^3)						
0	0.765 ± 0.053	0.779 ± 0.050	0.780 ± 0.058	0.807 ± 0.025	0.580	0.952 ± 0.056††
	(1.532 ± 0.067)	(1.591 ± 0.078)	(1.620 ± 0.082)	(1.572 ± 0.063)	(0.319)	(1.935 ± 0.119††)
0.48	0.843 ± 0.017	0.902 ± 0.024	1.015 ± 0.049*	1.003 ± 0.054*	<0.0001	1.168 ± 0.044††
	(1.779 ± 0.040)	(1.953 ± 0.115)	(2.294 ± 0.181*)	(2.325 ± 0.151*)	(<0.0001)	(2.600 ± 0.051††)
0.94	0.893 ± 0.045†	1.008 ± 0.047†	1.124 ± 0.018†	1.235 ± 0.038†	<0.0001	1.224 ± 0.071††
	(1.867 ± 0.131†)	(2.325 ± 0.094†)	(2.785 ± 0.153†)	(4.105 ± 0.166†)	(<0.0001)	(2.610 ± 0.164††)
1.01	0.869 ± 0.037†	1.050 ± 0.032*	1.105 ± 0.044*	1.285 ± 0.045†	<0.0001	1.239 ± 0.048††
	(1.793 ± 0.063†)	(2.343 ± 0.050†)	(2.746 ± 0.134†)	(4.465 ± 0.107†)	(<0.0001)	(2.683 ± 0.100††)
1.20	0.892 ± 0.071†	1.026 ± 0.021*	1.097 ± 0.042*	1.280 ± 0.031†	<0.0001	1.247 ± 0.031††
	(1.862 ± 0.169†)	(2.353 ± 0.033†)	(2.748 ± 0.102†)	(4.033 ± 0.237†)	(<0.0001)	(2.615 ± 0.066††)
1.41	0.868 ± 0.041†	1.046 ± 0.016*	1.097 ± 0.063*	1.317 ± 0.040†	<0.0001	1.180 ± 0.063††
	(1.795 ± 0.119†)	(2.316 ± 0.033†)	(2.607 ± 0.182†)	(3.969 ± 0.099†)	(<0.0001)	(2.412 ± 0.117)
2.17	0.879 ± 0.030†	1.016 ± 0.035†	1.152 ± 0.056†	1.343 ± 0.061†	<0.0001	1.131 ± 0.046††
	(1.781 ± 0.062†)	(2.138 ± 0.083†)	(2.536 ± 0.075†)	(3.578 ± 0.091†)	(<0.0001)	(2.332 ± 0.126††)
2.17 (AC)		0.993 ± 0.029				
		(2.079 ± 0.097)				
2.17 (AC + SC)		0.951 ± 0.036**				
		(1.983 ± 0.080**)				

Data are expressed as mean ± 1 standard deviation (mm) of 5 measurements

ANOVA analysis of variance, *AC* attenuation correction, *SC* scatter correction

* $P < 0.05$ vs. ^{18}F

† $P < 0.05$ vs. other radionuclides

†† $P < 0.05$ vs. ^{11}C at the center of field of view by *t* test

** $P < 0.05$ vs. ^{11}C FWHM or FWTM value with material density of 2.17 g/cm^3

cm^3). By contrast, the FWTM/FWHM ratio of low energy-emitting radionuclides such as ^{18}F was stable over the entire range of material density tested. The ^{11}C source placed 25 mm off-center showed FWTM/FWHM ratios similar to those obtained at the center of FOV. The relationship between FWHM/FWTM and mean energy of the 4 radionuclides are plotted for various surrounding materials in Figs. 3 and 4. The FWHM values were not different among the radionuclides at low material densities (material density 0–0.48 g/cm^3), but showed close correlations at middle to high material densities (material density 0.94–2.17 g/cm^3). Essentially similar results were observed for the FWTM values (Fig. 4).

EP resolution phantom study

Figure 5 depicts EP resolution phantom images for ^{18}F, ^{11}C, and ^{13}N. By visual inspection, 1.8, 1.5, and 1.3 mm rods were clearly visible for ^{18}F, whereas 1.0 mm or smaller rods were difficult to identify. The rod visibility for ^{11}C was slightly worse than that for ^{18}F. For ^{13}N, even 1.8 mm or 1.5 mm rods were blurred as compared with those for ^{18}F or ^{11}C.

Concentric ring paper phantom

CT and PET images of a concentric ring paper phantom are presented in Fig. 6. For ^{18}F, the most inner layer (layer 1), which was approximately 7.5-mm apart from the ^{18}F source, was clearly visualized, whereas outer layers (layers 2–4) were only faintly or not visible. When the ^{18}F source was covered with 3-mm thick clay, none of the layers was visible. For ^{11}C and ^{13}N, the second inner layer (layer 2) was faintly visible in addition to the more clearly visible layer 1. For ^{15}O, even the outer layers (layers 3 and 4) were visible in addition to layers 1 and 2. These visual observations were confirmed by quantitative analysis of layer-to-center count ratios summarized in Table 3. When the ^{18}F source was placed in air without the clay cover, the count ratio in layer 1 was 0.279 ± 0.093 and decreased as a function of layer number. With the clay cover, the count ratio was only 0.003 ± 0.001 in layer 1 and dropped to 0 in

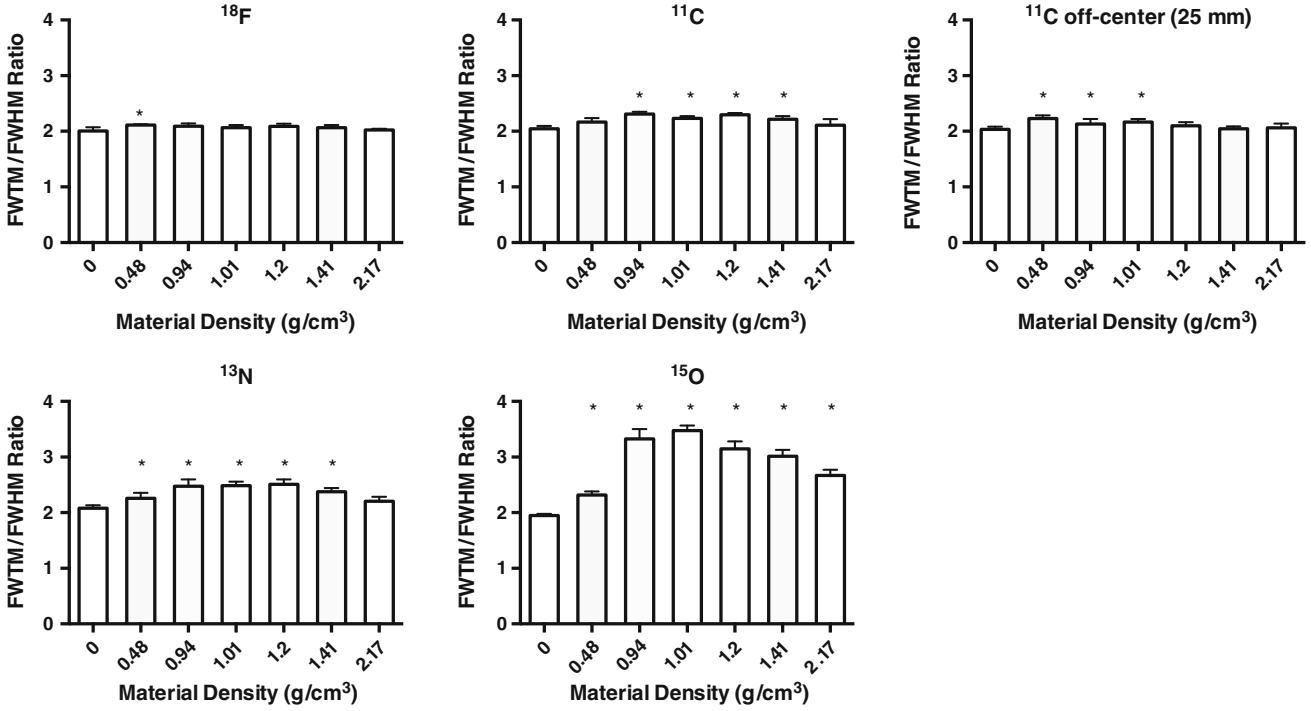

Fig. 2 The full-width at tenth of maximum to full-width at half-maximum (FWTM/FWHM) ratios plotted for ^{18}F (*upper left*), ^{11}C (*upper middle*), off-centered ^{11}C by 25 mm (*upper right*), ^{13}N (*lower left*), and ^{15}O (*lower middle*) as a function of surrounding material density (g/cm^3). *Error bar* indicates standard deviation. *$P < 0.05$ vs. FWTM/FWHM ratio at material density 0 g/cm^3

outer layers. Significantly higher layer-to-center ratios than for ^{18}F were observed in outer layers for ^{15}O.

The relationships between mean energy of positron emitters and mean of layer-to-center count ratios in each layer are plotted in Fig. 7. The inner layers (layers 1 and 2) did not show significant correlations with energy of radionuclides, whereas the outer layers (layers 3 and 4) showed significant correlations between the two parameters.

Discussion

To the best of our knowledge, this is the first study reporting the effect of surrounding materials on IR-RF of 4 commonly used positron emitters in experimental phantoms. The major findings of this study were that (1) when the radionuclides were placed in air (material density 0 g/cm^3), IR-RFs expressed as FWHM or FWTM were similar among the radionuclides tested; (2) as the material density increased, IR-RFs for higher energy-emitting radionuclides (^{11}C, ^{13}N, and ^{15}O) became worse, whereas those of ^{18}F remained relatively constant over the range of surrounding material densities tested (0–2.17 g/cm^3); (3) the FWTM/FWHM ratio of high energy-emitting radionuclides such as ^{15}O increased as a function of material density, which was followed by subsequent decrease at high material densities (1.2–2.17 g/cm^3); (4) both FWHM and FWTM values were closely correlated with mean energy of radionuclides at middle to high material densities (material density 0.94–2.17 g/cm^3); (5) EP resolution phantom images for ^{18}F, ^{11}C, and ^{13}N confirmed the observation mentioned above; and (6) using a concentric ring paper phantom, annihilations outside the source were visible and measurable.

Iterative reconstruction-based line-source response function and surrounding materials

Differences in spatial resolution due to different positron range have been reported in 1970s [11–13]. More recently, Disselhorst et al. [14] have reported poorer spatial resolutions for high energy positron emitters (^{68}Ga, ^{124}I) as compared with those for low energy positron emitters (^{18}F, ^{89}Zr). However, these measurements were mostly performed only in water. It should also be noted that organs in living animals are rather complicated in that they often consist of various tissues such as air, adipose, water, and bone. Our results demonstrated that, when the radioactive source was placed in air, there were no significant differences in IR-RF expressed as FWHM or FWTM among radionuclides tested. Furthermore, IR-RF was better in air

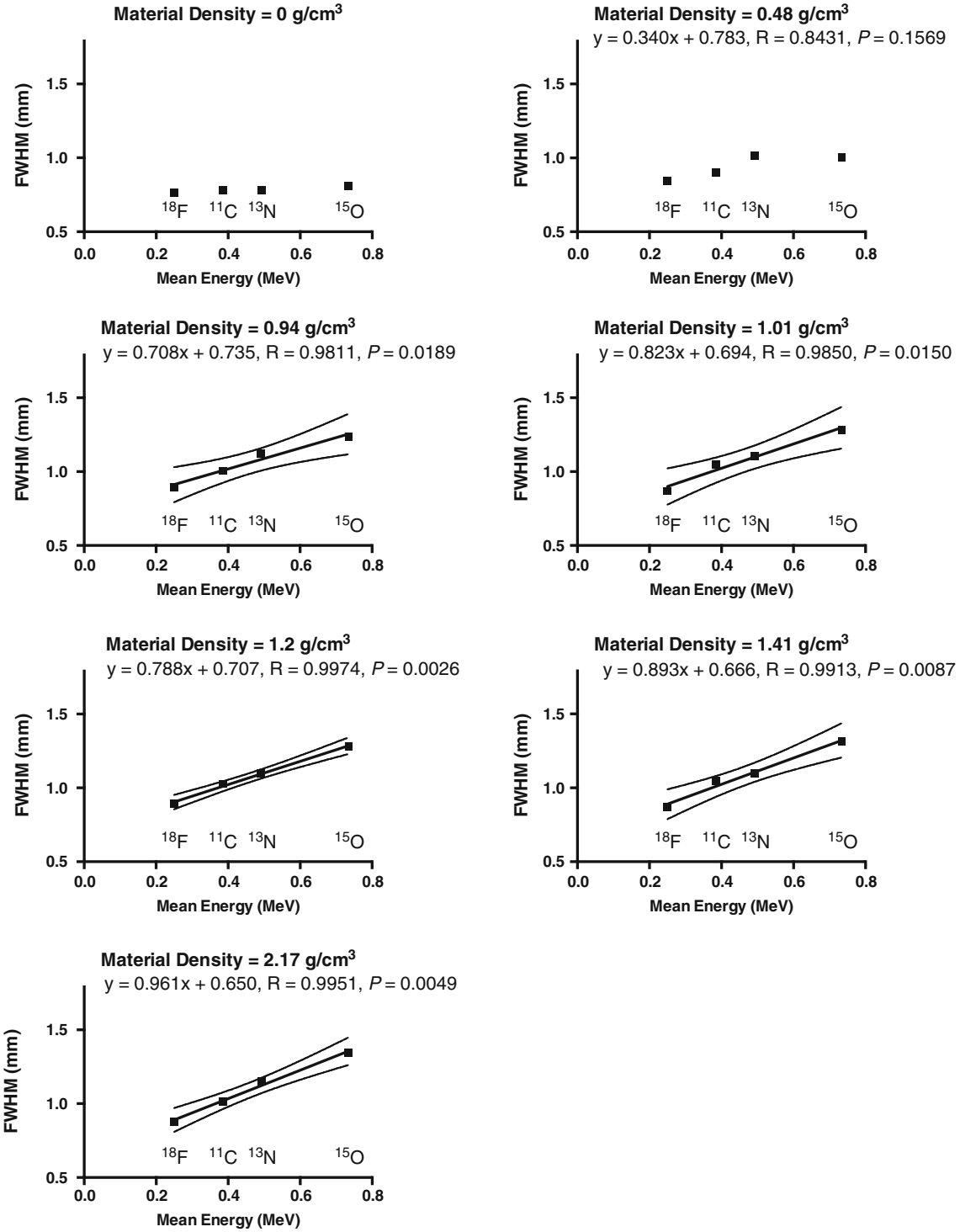

Fig. 3 *Scatter plots* showing the relationship between iterative reconstruction-based line-source response function expressed as full-width half-maximum (FWHM) and mean energy of ^{18}F, ^{11}C, ^{13}N, and ^{15}O for various surrounding materials. *Solid lines* indicate regression line, *dot lines* 95 % confidence intervals

than in tissue materials for all radionuclides. This is different from what was expected from the results of MonteCarlo simulation [4], where spatial resolution worsened as a function of tissue density, but is consistent with an experimental study [5], where spatial resolution in air was better than that in water or lung simulated tissue. We also observed that each radionuclide had different material density which produced the worst FWHM or FWTM. As

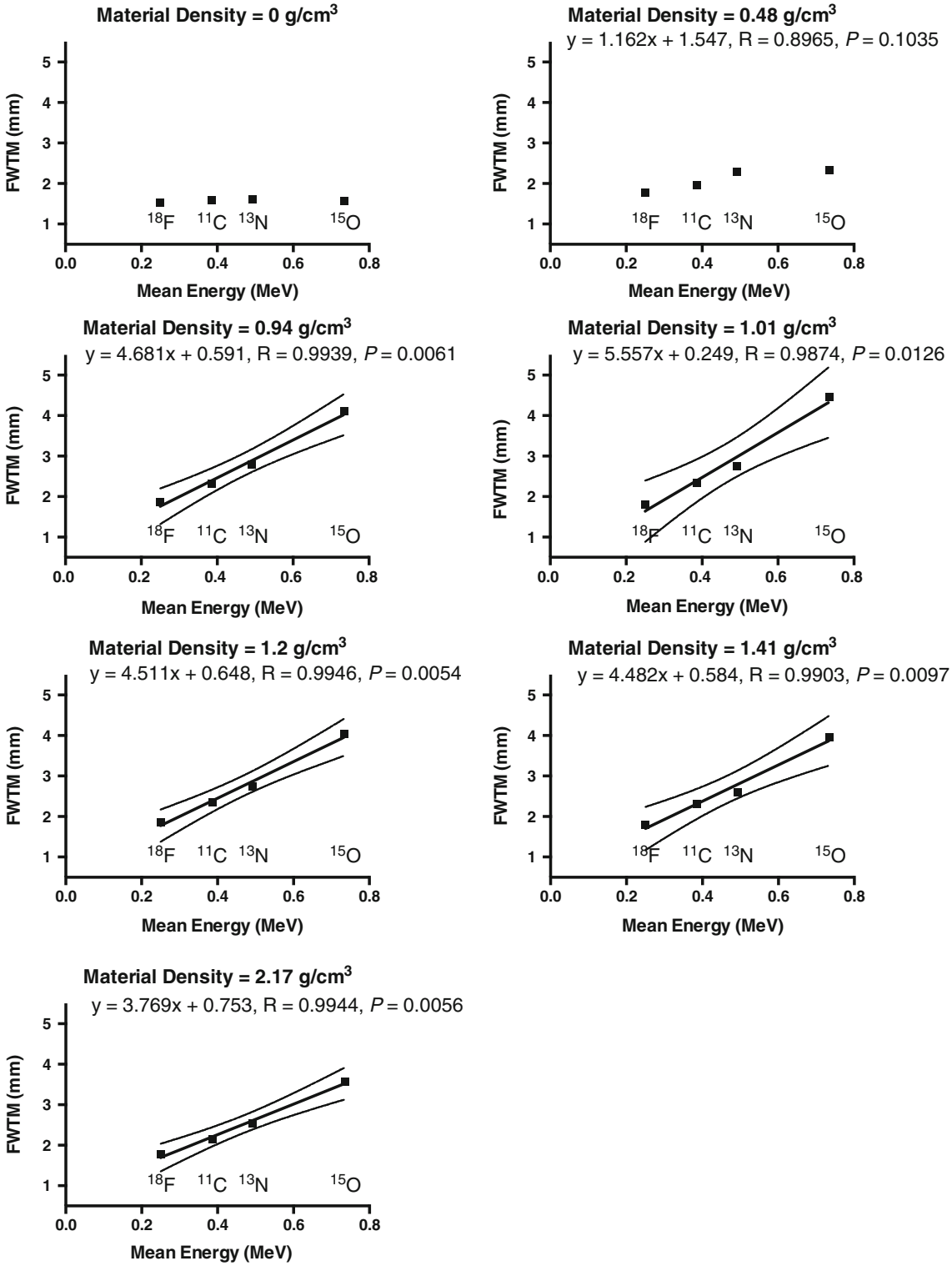

Fig. 4 *Scatter plots* showing the relationship between iterative reconstruction-based line-source response function expressed as full-width tenth maximum (FWTM) and mean energy of ^{18}F, ^{11}C, ^{13}N, and ^{15}O for various surrounding materials. *Solid lines* indicate regression line, *dot lines* 95 % confidence intervals

mentioned in that study, once a positron leaves the source in air, it is likely to escape detection because the flight range in air is several meters. Thus, only the annihilations within the source are detected in air. With the increase in material density, however, more positrons are likely to be trapped within the surrounding materials, but some may

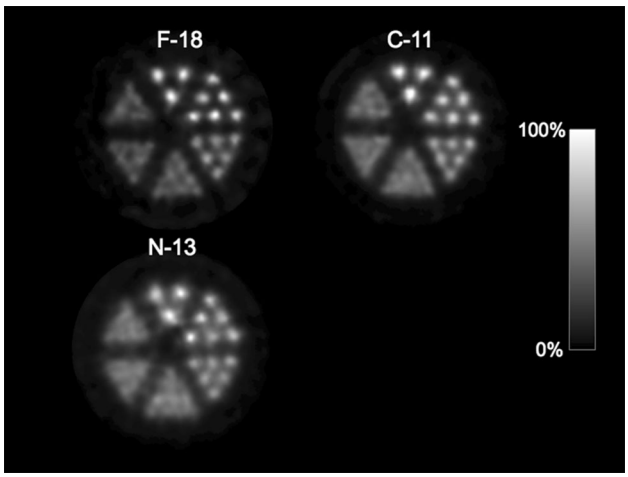

Fig. 5 EP resolution phantom images with fillable capillary rods of 0.7, 0.9, 1.0, 1.3, 1.5, and 1.8 mm in diameter for ^{18}F, ^{11}C, and ^{13}N. Images were normalized to the peak activity on each image

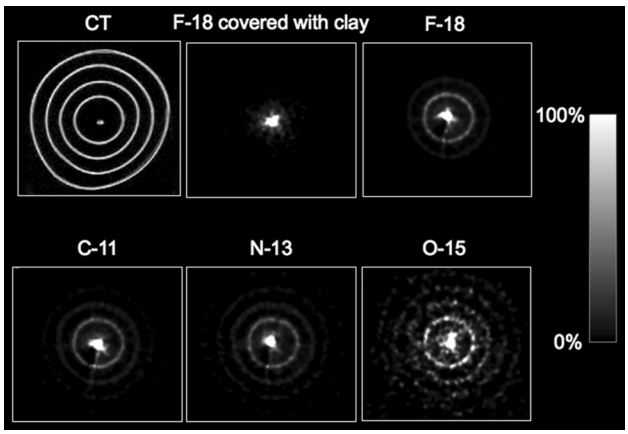

Fig. 6 CT (*upper left*) and PET images of a concentric ring paper phantom for ^{18}F with (*upper middle*) and without clay cover (*upper right*), ^{11}C (*lower left*), ^{13}N (*lower middle*), and ^{15}O (*lower right*). The PET images are normalized to the mean of central source activity

travel long distance depending on the energy of positron emitters, resulting in worsening in FWHM and FWTM. Furthermore, this may result in long tail distribution of positron range with high energy-emitting radionuclides, and may explain the worsened FWTM/FWHM ratio at low to middle material density (0.48–1.01 g/cm^3) particularly with ^{13}N and ^{15}O. When the material density is high, most positrons are likely to annihilate near the source, resulting in lessened both FWHM and FWTM, which was true for low energy-emitting radionuclides (^{18}F and ^{11}C). For high energy-emitting radionuclides, some positrons may still travel long distance even in high density materials, which may explain the worst FWHM observed at the material density of 2.17 g/cm^3 for ^{13}N and ^{15}O. However, the majority of positrons seem to be trapped near the source even for these radionuclides, resulting in Gaussian-like distribution rather than long tail distribution of positron range. This was reflected by lessened FWTM and FWTM/FWHM ratio at high density materials observed in this study. Our results also showed that both FWHM and FWTM for higher energy positron emitters were variable depending on surrounding material density, whereas those for ^{18}F remained relatively constant. This indicates that surrounding material affects IR-RF particularly for high energy positron emitters. To this end, IR-RF is mainly determined by the energy of positron emitters when the source is surrounded by dense materials as illustrated in Figs. 3 and 4. Thus, IR-RF as measured by a preclinical PET is highly dependent on surrounding materials and the energy of positron emitters. It would be worthwhile to mention on the IR-RF values reported in this study, which seem to be better than those reported for the preclinical PET system [3, 6, 15]. This is likely because we used a very thin (0.14-mm in inner diameter) capillary phantom, and because we used an iterative reconstruction rather than filtered back projection, which reflects our routine practice. It should also be noted that iterative reconstruction may overestimate the resolution, which is known to occur as described in a study by de Jong et al. [16]. The results obtained by off-centered ^{11}C source showed that there was only modest deterioration in both FWHM and FWTM as compared to those by centered ^{11}C source, indicating that FWHM/FWTM values are rather stable over transaxial FOV. This is consistent with published data [6] reporting

Table 3 Layer-to-center count ratios with a concentric ring paper phantom for ^{18}F, ^{11}C, ^{13}N, and ^{15}O

	^{18}F with clay	^{18}F	^{11}C	^{13}N	^{15}O	*P* value
Layer 1	0.003 ± 0.001*	0.279 ± 0.093	0.233 ± 0.058	0.175 ± 0.062	0.266 ± 0.051	<0.0001
Layer 2	0.000 ± 0.000*	0.082 ± 0.029	0.104 ± 0.030	0.087 ± 0.033	0.150 ± 0.038†	<0.0001
Layer 3	0.000 ± 0.000	0.019 ± 0.010	0.043 ± 0.012	0.048 ± 0.020	0.098 ± 0.027*	<0.0001
Layer 4	0.000 ± 0.000	0.002 ± 0.003	0.022 ± 0.005†	0.027 ± 0.011†	0.069 ± 0.020*	<0.0001

Data are expressed as mean ± 1 standard deviation (mm) of 5 measurements

* $P < 0.05$ vs. other groups

† $P < 0.05$ vs. ^{18}F

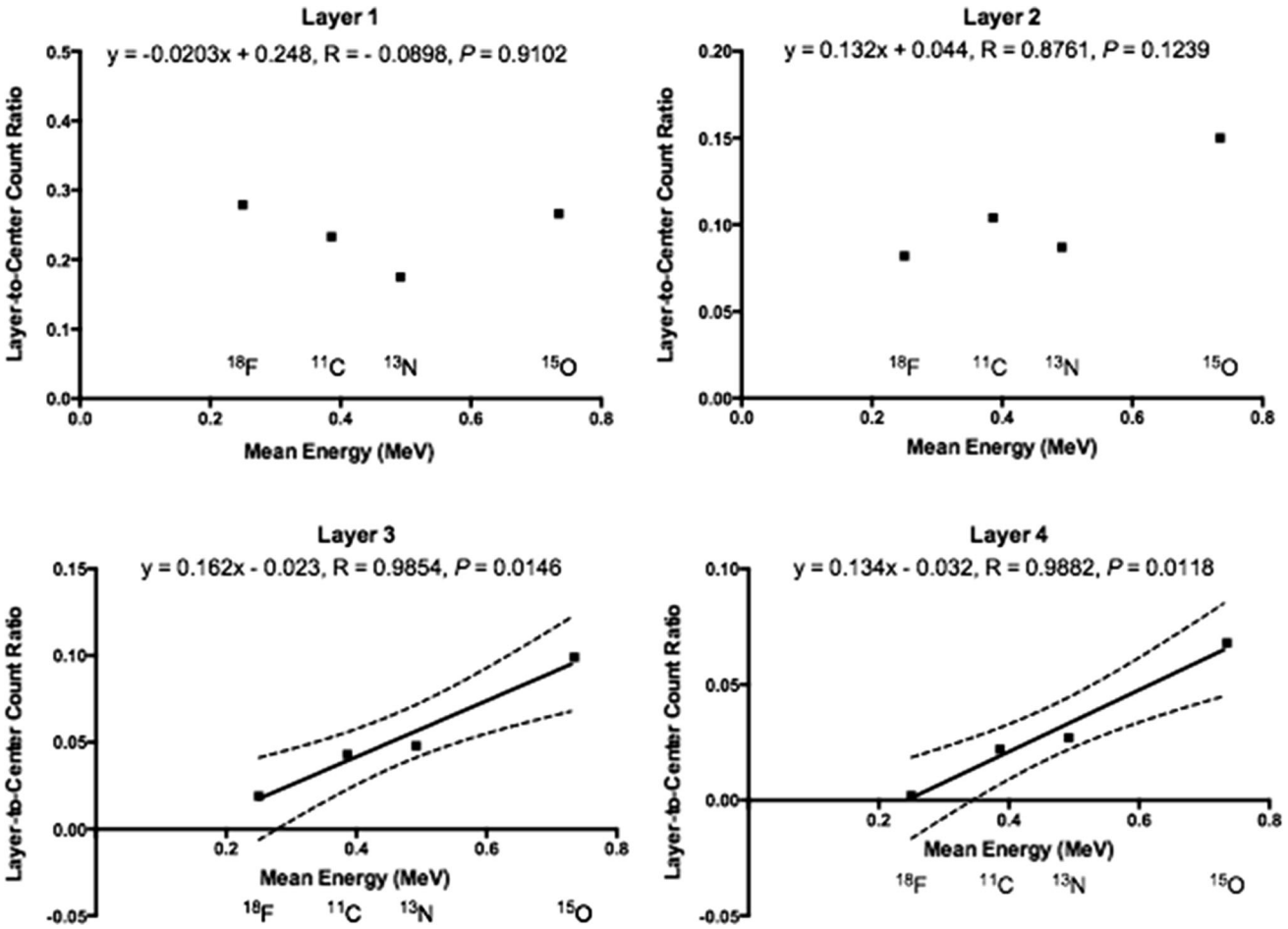

Fig. 7 The relationships between mean energy of positron emitters and mean of layer-to-center count ratios in each layer. *Solid lines* indicate regression line, *dot lines* 95 % confidence intervals

the performance of the same preclinical PET scanner to ours, where relatively stable FWHM/FWTM values over transaxial FOV were observed with the use of iterative reconstruction.

The use of attenuation and scatter correction slightly but significantly improved IR-RF as reflected by FWHM or FWTM in the presence of high density surrounding material, whereas the use of attenuation correction alone did not. This indicates that the presence of scatter may unfavorably affect IR-RF by adding counts that come from materials surrounding the source. Because the attenuation/scatter correction software in the LabPET system has become available very recently and still needs validation, we did not systemically looked at the effects of attenuation/scatter correction on IR-RF in the present study. Nevertheless, this issue needs to be addressed by further studies.

EP resolution phantom results with material density of 1.19 g/cm^3 are essentially consistent with the observation described above in that IR-RF for high energy-emitting radionuclides such as ^{13}N is worse than that for low energy-emitting radionuclides such as ^{18}F. At the same time, it should be noted that, although such a resolution phantom image gives an estimate of IR-RF in a certain situation, it does not necessarily reflect IR-RF in reality, where a radioactive source can be surrounded by various tissues.

Annihilations outside the source

Theoretically, a positron emitter travels for a distance depending on its energy before annihilation and, therefore, annihilation may occur outside the source. As mentioned earlier, the travel range of a positron could reach several meters in air [5]. In the presence of light materials such as paper layer, some positrons should be trapped by them with annihilations, which could be detected using a preclinical PET camera. The results of the concentric ring paper phantom study demonstrated that such annihilations outside the radio-active source are clearly visible, although the image quality of ^{15}O image was somewhat poor as

compared to those of ^{18}F or ^{11}C, reflecting relatively lower dose and shorter acquisition time for ^{15}O. Furthermore, when the source was covered with clay to stop positron flight, none of the layers was visible, which was confirmed by the quantitative analysis of layer-to-center count ratios. This indicates that layer visibility was due to annihilations in that layer and not the result of scattering of emitted gamma-ray following annihilation.

Our results also showed that annihilations in layers near the central source were visible with all radionuclides tested, whereas those in distant layers were visible only with high-energy radionuclides such as ^{15}O. Moreover, the amount of annihilations in distant layers was mainly determined by the energy level of positron emitters. Thus, visibility of such annihilations depends on the distance between the source and object, and type of radionuclide. From a viewpoint of in vivo imaging, our results suggest that annihilations outside the source may constitute an imaging artifact in some rodent organs that contain tissue and air in face-to-face such as those encountered in gastrointestinal system or oral cavity. However, this needs to be addressed in further in vivo studies.

Conclusions

The results indicate that surrounding material affects IR-RF particularly for high energy positron emitters. Furthermore, annihilation outside the radio-active source can be visualized with some circumstances such as those seen with a concentric ring paper phantom.

Acknowledgments This work was supported by Ishikawa prefectural government.

Conflict of interest None of the authors has conflicts to disclose.

References

1. Bravo PE, Bengel FM. The role of cardiac PET in translating basic science into the clinical arena. J Cardiovasc Transl Res. 2011;4:425–36.
2. de Kemp RA, Epstein FH, Catana C, Tsui BM, Ritman EL. Small-animal molecular imaging methods. J Nucl Med. 2010;51(Suppl 1):18S–32S.
3. Goertzen AL, Bao Q, Bergeron M, Blankemeyer E, Blinder S, Canadas M, et al. NEMA NU 4-2008 comparison of preclinical PET imaging systems. J Nucl Med. 2012;53:1300–9.
4. Sanchez-Crespo A, Andreo P, Larsson SA. Positron flight in human tissues and its influence on PET image spatial resolution. Eur J Nucl Med Mol Imaging. 2004;31:44–51.
5. Kemerink GJ, Visser MG, Franssen R, Beijer E, Zamburlini M, Halders SG, et al. Effect of the positron range of ^{18}F, ^{68}Ga and ^{124}I on PET/CT in lung-equivalent materials. Eur J Nucl Med Mol Imaging. 2011;38:940–8.
6. Prasad R, Ratib O, Zaidi H. NEMA NU-04-based performance characteristics of the LabPET-8 small animal PET scanner. Phys Med Biol. 2011;56:6649–64.
7. Health Physics Society (HPS). Radionuclide Decay Data. 2010.
8. International Commission on Radiation Units and Measurements (ICRU). Stopping Powers for Electrons ans Positrons. ICRU report 37: ICRU; 1984.
9. NEMA Standards Publication NU 4-2008: Performance Measurements of Small Animal Positron Emission Tomographs. Rosslyn, VA: National Electrical Manufacturers Association; 2008.
10. Loening AM, Gambhir SS. AMIDE: a free software tool for multimodality medical image analysis. Mol Imaging. 2003;2:131–7.
11. Cho ZH, Chan JK, Ericksson L, Singh M, Graham S, MacDonald NS, et al. Positron ranges obtained from biomedically important positron-emitting radionuclides. J Nucl Med. 1975;16:1174–6.
12. Phelps ME, Hoffman EJ, Huang SC, Ter-Pogossian MM. Effect of positron range on spatial resolution. J Nucl Med. 1975;16:649–52.
13. Derenzo SE, Budinger TF. Resolution limit for positron-imaging devices. J Nucl Med. 1977;18:491–2.
14. Disselhorst JA, Brom M, Laverman P, Slump CH, Boerman OC, Oyen WJ, et al. Image-quality assessment for several positron emitters using the NEMA NU 4-2008 standards in the Siemens Inveon small-animal PET scanner. J Nucl Med. 2010;51:610–7.
15. Prasad R, Ratib O, Zaidi H. Performance evaluation of the FLEX triumph X-PET scanner using the national electrical manufacturers association NU-4 standards. J Nucl Med. 2010;51:1608–15.
16. de Jong HW, van Velden FH, Kloet RW, Buijs FL, Boellaard R, Lammertsma AA. Performance evaluation of the ECAT HRRT: an LSO-LYSO double layer high resolution, high sensitivity scanner. Phys Med Biol. 2007;52:1505–26.